Effects of Gold Substrates on the Intrinsic and Extrinsic Activity of High-Loading Nickel-Based Oxyhydroxide Oxygen Evolution Catalysts

Chakthranont, Pongkarn; Kibsgaard, Jakob; Gallo, Alessandro; Park, Joonsuk; Mitani, Makoto; Sokaras, Dimosthenis; Kroll, Thomas; Sinclair, Robert; Mogensen, Mogens Bjerg; Jaramillo, Thomas F.

Published in:
A C S Catalysis

Link to article, DOI:
10.1021/acscatal.7b01070

Publication date:
2017

Document Version
Peer reviewed version

Effects of Gold Substrates on the Intrinsic and Extrinsic Activity of High-Loading Nickel-Based Oxyhydroxide Oxygen Evolution Catalysts

*Pongkarn Chakthranont[1], Jakob Kibsgaard[1,2,3], Alessandro Gallo[1,2], Joonsuk Park[4], Makoto Mitani[1], Dimosthenis Sokaras[5], Thomas Kroll[5], Robert Sinclair[4], Mogens B. Mogensen[6], and Thomas F. Jaramillo[1,2]**

AUTHOR ADDRESS

[1] SUNCAT Center for Interface Science and Catalysis, Department of Chemical Engineering, Stanford University, Stanford, California 94305, United States.

[2] SUNCAT Center for Interface Science and Catalysis, SLAC National Accelerator Laboratory, Menlo Park, California 94025, United States.

[3] Department of Physics, Technical University of Denmark, DK-2800 Kongens Lyngby, Denmark.

[4] Department of Materials Science and Engineering, Stanford University, 496 Lomita Mall, California 94305, United States

[5] Stanford Synchrotron Radiation Lightsource, SLAC National Accelerator Laboratory, 2575 Sand Hill Road, Menlo Park, 94025, California, United States

[6] Department of Energy Conversion and Storage, Technical University of Denmark, Frederiksborgvej 399, DK-4000 Roskilde, Denmark

KEYWORDS: substrate effects, oxygen evolution reaction, nickel oxyhydroxide, nickel cerium, nickel iron, loading dependence, conductivity, electrochemical impedance spectroscopy

ABSTRACT

We systematically investigate the effects of Au substrates on the oxygen evolution activities of cathodically electrodeposited nickel oxyhydroxide (NiOOH), nickel-iron oxyhydroxide (NiFeOOH), and nickel-cerium oxyhydroxide (NiCeOOH) at varying loadings from 0 – 2000 nmol of metal/cm^2. We determine that the geometric current densities, especially at higher loadings, were greatly enhanced on Au substrates: NiCeOOH/Au reached 10 mA/cm^2 at 259 mV overpotential, and NiFeOOH/Au achieved 140 mA/cm^2 at 300 mV overpotential, which were much greater than those of the analogous catalysts on graphitic carbon (GC) substrates. By performing a loading quantification using both inductively coupled plasma optical emission spectrometry and integration of the $Ni^{2+/3+}$ redox peak, we show that the enhanced activity is predominantly caused by the stronger physical adhesion of catalysts on Au. Further characterizations using impedance spectroscopy and *in situ* X-ray absorption spectroscopy revealed that the catalysts on Au exhibited lower film resistances and higher number of electrochemically active metal sites. We attribute this enhanced activity to a more homogeneous electrodeposition on Au, yielding catalyst films with very high geometric current densities on flat

substrates. By investigating the mass and site specific activities as a function of loading, we bridge the practical geometric activity to the fundamental intrinsic activity.

1. Introduction

The oxygen evolution reaction (OER) is the most important counter reaction for a large number of electrochemical energy conversions in aqueous environment, e.g. for H_2 production from water splitting, CO_2 reduction to hydrocarbons and oxygenates, NH_3 synthesis from N_2 reduction, H_2O_2 generation from O_2, and charging of metal-air batteries, all of which are promising for renewable energy storage and/or conversion to fuels and chemicals.[1-5] Depending on the application, the required current density for the reaction can vary by several orders of magnitude. For example, in photoelectrochemical water splitting, a geometric current density of 10 mA/cm^2 corresponds to approximately 10% solar-to-hydrogen efficiency and is considered a standard performance metric that is also used for the OER research.[6] However, for alkaline and proton-exchange membrane electrolyzers, the operating current densities are much higher, 0.5 and 2 A/cm^2, respectively.[7-8] Despite decades of research, a significant overpotential is required to drive the sluggish kinetics of the OER and only a few reports have demonstrated catalysts that achieve 500 mA/cm^2 at moderate overpotentials of less than 300 mV.[9-10] The lack of highly active OER catalysts on the geometric scale imposes a bottleneck in the commercialization of the electrochemical devices.[11]

Catalysts that can achieve high geometric activity must have both high intrinsic activity and a large number of active sites. The intrinsic activity of the catalyst depends on the binding energy of the OER intermediates, which can be tuned by chemical and electronic modifications of the active sites.[12] The number of active sites can be increased by loading more catalyst and/or nanostructuring to increase the electrochemically active surface area.[13-14] The challenge in attaining high geometric

activity arises from the entanglement between the intrinsic activity and the number of active sites of a catalyst. As the number of active sites increases, the intrinsic activity per site often decreases due to ohmic losses from increased loading or mass transport limitations caused by nanostructuring.[15] Hence, scaling up a catalyst for electrolyzer applications that operate at high geometric current density requires optimizing both intrinsic activity and number of active sites. This can only be accomplished with a thorough understanding of how intrinsic activity changes as a function of loading.

Nickel oxyhydroxide (NiOOH)-based catalysts are promising materials that can potentially achieve high geometric activity due to the outstanding intrinsic activity and the large intrinsic surface area.[16-17] Even though the intrinsic activity of NiOOH is low, it can be greatly improved by alloying with Fe or Ce.[18] Specifically, nickel-iron oxyhydroxide (NiFeOOH) and nickel-cerium oxyhydroxide (NiCeOOH) catalysts have proven to be active and robust, achieving 10 mA/cm^2 at overpotentials well below 300 mV.[19-21] NiOOH-based catalysts also exhibit a large surface area due to its layered structure, allowing this catalyst to behave to some extend as a "volume" catalyst where the overall activity scales with the mass loading.[22-23] Furthermore, a high surface area support, such as nickel foam, has been proven effective for increasing the surface area of NiOOH-based catalysts without significant mass transport limitations.[24] Nevertheless, there remains significant room for improvement especially at the high geometric current densities.

One strategy that can potentially improve the intrinsic activity and increase the number of active sites of NiOOH-based catalysts is by favorable support interactions. There is no standardized substrate for OER testing. Various supports have been used such as glassy carbon (GC), fluorine doped tin oxide (FTO), indium doped tin oxide (ITO), Pt, Pd, carbon paper, nickel foam, and Au.[25-32] It has been widely reported that Au substrates can enhance the activity of submonolayer

transition metal oxide OER catalysts such as Ni, Co, Fe, and Mn oxides either by electronic structure modification of the active sites or by direct participation in the reaction.[27-28, 33-36] Recently, we have also discovered that Au substrates drastically enhance the geometric activity of NiOOH-based catalysts, especially NiCeOOH synthesized by cathodic electrodeposition, which can be fabricated to a highly active and stable OER electrode.[19] The intrinsic activity at various loadings of NiFeOOH deposited on Au has been investigated;[22] there is much to be learned about the effect of Au substrates on the activity of high loading catalysts, especially because high loading systems are more likely to be implemented in practical devices.

In this work, we present a systematic investigation of the effect of two flat substrates, Au and GC, on the geometric activity, intrinsic activity, and number of active sites of NiOOH, NiFeOOH, and NiCeOOH OER catalysts. We demonstrate that the NiOOH-based catalysts on Au performed exceptionally better relative to those on GC substrate, achieving much higher geometric current densities at high catalyst loadings. Specifically, NiCeOOH/Au was able to achieve 10 mA/cm^2 at overpotential as low as 259 mV. At 300 mV overpotential, NiFeOOH/Au performed the best, achieving a geometric current density of 140 mA/cm^2 in 1 M Fe-free NaOH. To understand the origins of the effect of Au and GC substrates, we employed inductively coupled plasma, integration of Ni redox peak, electrochemical impedance spectroscopy, *in situ* X-ray absorption spectroscopy, and cross-sectional transmission electron microscopy. We attribute the superior geometric activity to the homogeneous distribution of catalyst deposited on Au compared to GC substrate, not to enhanced intrinsic activity. The use of Au substrates allows for (1) a greater amount of catalyst physically adhered and electrically connected, (2) a lower film resistivity, and (3) a higher number of electrochemically active sites. These effects are critical to the performance

of NiOOH, NiFeOOH, and especially NiCeOOH, where over 6-fold increases in geometric current density at 300 mV overpotential can be achieved on Au compared to GC substrate.

2. Experimental Section

2.1 Synthesis of NiOOH, NiFeOOH, and NiCeOOH

NiOOH, NiFeOOH, and NiCeOOH were synthesized by electrodeposition from metal nitrate aqueous solutions using $Ni(NO_3)_2 \cdot 6H_2O$ (99.9985%, Strem Chemicals), $Fe(NO_3)_3 \cdot 9H_2O$ (99.95%, Sigma-Aldrich), and $Ce(NO_3)_3 \cdot 6H_2O$ (99.99%, Sigma-Aldrich). The GC disk substrates (0.196 cm^2 geometric area, SIGRADUR G HTW Hochtemperatur-Werkstoffe GmbH) were polished and sonicated sequentially in acetone and isopropanol to clean off organic contaminants. The cleaned substrates were further soaked in 10% nitric acid to leech metal contaminants. The Au substrates were prepared by e-beam evaporating 10 nm of Ti as a sticking layer and 100 nm of Au on the cleaned GC disks. Electrodeposition was carried out in a three-electrode configuration with a rotating disk electrode (RDE) setup using a carbon rod counter electrode and a Ag/AgCl reference electrode. The glass container, the counter electrode, the reference electrode, and the Teflon holder for the GC disk were prewashed in 10% nitric acid to mitigate metal contamination. The deposition electrolytes were 100 mM Ni for NiOOH, 95 mM Ni and 5 mM Fe for NiFeOOH, and 95 mM Ni and 5 mM Ce for NiCeOOH. The deposition current of $-16\ mA/cm^2$ was passed at varying deposition times from 1 – 30 s at a rotating speed of 400 rpm, similar to the previous reported work (see further discussion in the SI).[18-19] The average deposition potentials for GC and Au substrates were -1.25 and -0.95 V and vs. Ag/AgCl, respectively (Figure S1) and the ohmic resistance was ~50 ohm as measured by impedance spectroscopy at 100 kHz. The deposited catalysts were rinsed

with water and dried in an air stream, and then they were tested for the electrochemical performance immediately to minimize further oxidation in air.

2.2 Electrochemical Characterizations and Analysis

Electrochemical evaluation was performed in a 1 M Fe-free sodium hydroxide (99.99%, Sigma-Aldrich) electrolyte which was purified according to a previously reported procedure[37] using $Ni(OH)_2$ to precipitate trace Fe. The electrochemical setup consisted of a polypropylene electrochemical cell, a Pt wire counter electrode, and a Teflon Hg/HgO reference electrode (CH Instruments), all of which were cleaned in 10% nitric acid to mitigate Fe contamination. The reference potential scale was calibrated to the reversible hydrogen electrode (RHE) using a Pt wire as the working electrode in a H_2-saturated electrolyte; all potentials are reported on the RHE scale. The electrochemical measurement consisted of an ohmic drop determination by electrochemical impedance spectroscopy (EIS) at open circuit potential and a 100 kHz AC-modulation of 10 mV amplitude. Compensating for 85% resistance, a cyclic voltammogram (CV) was scanned at 10 mV/s from 1.23 V vs RHE to 1.70, 1.55, and 1.60 V vs RHE for NiOOH, NiFeOOH, and NiCeOOH, respectively. The CV was followed by an EIS scan from 200 kHz to 20 mHz at the most anodic potential from the CV scan of each catalyst. Each CV was further compensated for the last 15% using the ohmic resistance value from the anodic EIS. The oxidation charge (area under the oxidation peak) were calculated from the 85% compensated CV, and the OER activity was obtained from the 100% compensated CV. Error analysis at each different condition was conducted by synthesizing and testing 2 – 5 repeat samples.

The impedance data was fitted by a nonlinear least-squares solver function in MATLAB to extract the circuit parameters: electrolyte resistance (R_e), film resistance (R_f), film constant phase element

(Q_f, a_f), charge transfer resistance (R_{ct}), and double layer constant phase element (Q_{dl}, a_{dl}). The parameters associated with a constant phase element were then converted to an average capacitance (see SI for detailed calculation).[38] The Tafel slope was also calculated from the R_{ct} and the current recorded during EIS measurement. Although mass transport could play a role in the case of thick oxide films, the Warburg impedance was neglected in this study for the simplicity of the model and the analysis. The R^2 values of all fits were all greater than 0.95.

2.3 Physical and Chemical Characterizations

The mass loading and elemental composition of both freshly prepared and electrochemically tested samples of NiOOH, NiFeOOH, and NiCeOOH were determined using inductively coupled plasma optical emission spectrometry (ICP-OES) (Thermo Scientific ICAP 6300 Duo View Spectrometer). Each set of catalyst films (9 different loadings for both Au and GC substrates) was dissolved in aqua regia (3 parts HCl:1 part HNO_3) overnight before dilution to 5% acid with Millipore water. Ni, Ce, Au, and Fe standards (Sigma-Aldrich) were used for calibration.

The oxidation state of NiCeOOH was further investigated by *in situ* high energy resolution fluorescence detected X-ray absorption spectroscopy (HERFD-XAS). The measurements were carried out at the Stanford Synchrotron Radiation Lightsource (SSRL). Both incident beam and fluorescence entered and exited through the silicon nitride window or GC wafer at the back of the electrodes at an angle of ~45°, with no penetration of electrolyte necessary. HERFD-XAS measurements were made with the high resolution spectrometer at the SSRL beamline 6−2.[39] The incident energy was selected using a double-crystal monochromator with Si(111) crystals for measurements at the Ni K-edge. A Rowland circle spectrometer (R = 1 m) was aligned to the peaks of the Ni Kα lines. The Ni Kα emission at 7478 eV was collected using three spherically bent

Si(620) crystals at a Bragg angle of 74.9°. The combined resolution of the spectrometer and monochromator was 1.3 eV for measurements at the Ni K-edge. HERFD XAS scans were treated by subtracting a constant background (typically ~25 counts/s) and normalized to an edge-jump of 1.

NiOOH and NiCeOOH were deposited for 1 s on GC wafers and Au coated Si_3N_4 windows and the catalysts were illuminated with X-ray from the back side through the substrate.[35] The XAS spectra were obtained under applied bias at 1.23 and 1.65 V vs RHE.

The surface chemical composition was investigated by X-ray photoelectron spectroscopy (XPS), and the crystallinity was assessed by X-ray diffraction (XRD) similar to previous work (not shown here).[19] The morphology of the NiCeOOH specifically was characterized by atomic force microscopy (AFM) in a noncontact mode (Park XE-70).

Cross-sectional transmission electron microscopy (TEM) samples were prepared using Focus Ion Beam (FIB, FEI Helios nanolab 600i) lift-off technique employing 30 kV Ga+ ion beam. High-resolution TEM imaging and scanning TEM energy dispersive x-ray spectroscopy (STEM-EDS) mapping were acquired using aberration-corrected TEM (FEI Titan ETEM 80-300) at 300 kV accelerating voltage.

3. Results and Discussion

3.1 Substrate Effects on the Geometric Activities of NiOOH, NiFeOOH, and NiCeOOH

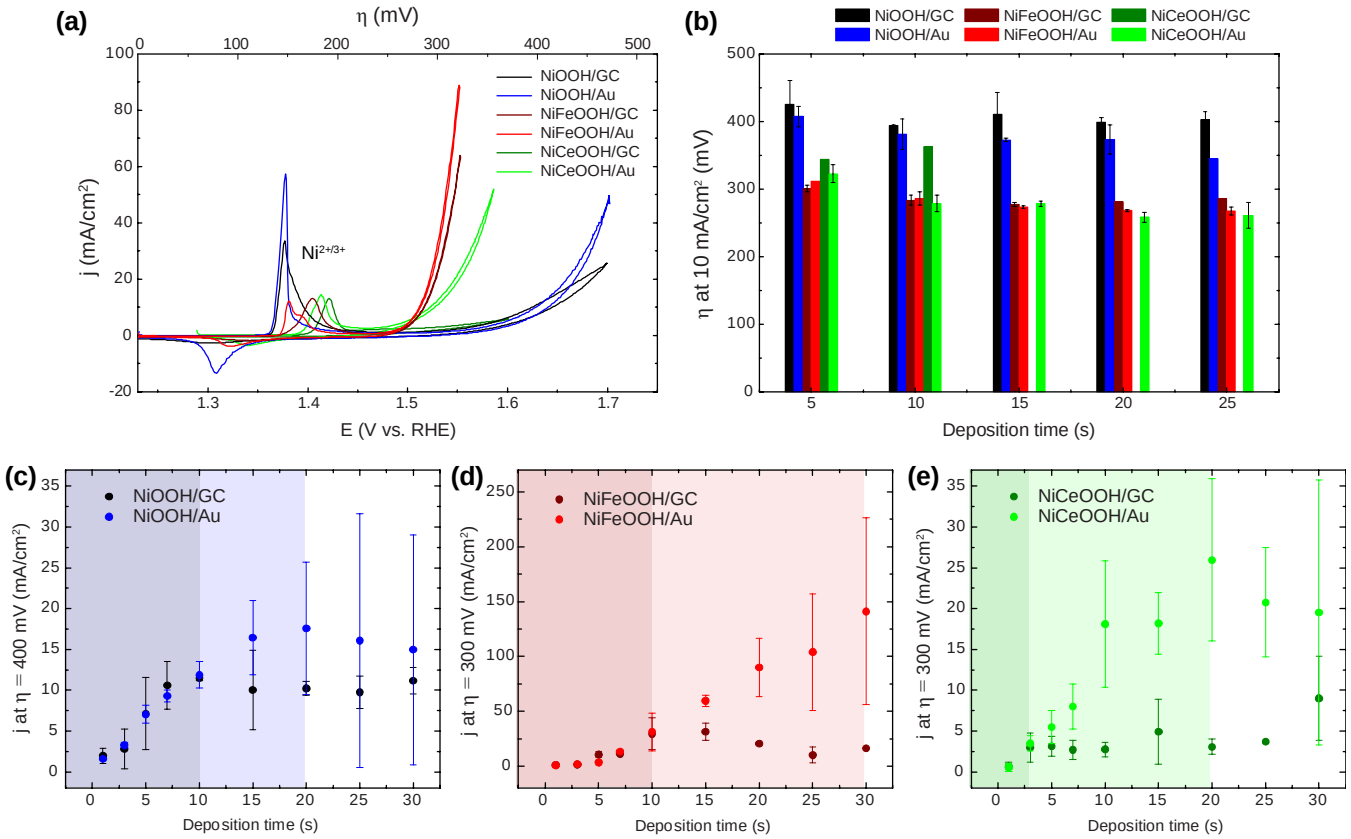

Figure 1. (a) CVs of NiOOH, NiFeOOH, and NiCeOOH on GC and Au substrates that were cathodically deposited at -16 mA/cm^2 for 10 s. (b) Overpotentials (η) required to achieve 10 mA/cm$^2_{geo}$ for catalysts with varying deposition time. The averaged oxygen evolution geometric current density as a function of deposition time of (c) NiOOH at 400 mV overpotential, (d) NiFeOOH at 300 mV overpotential, and (e) NiCeOOH at 300 mV overpotential. The highlighted areas signify the linear regime where the OER current density scales linearly with the deposition time. The lighter colors are for Au substrates, and darker colors are for GC substrates. The nonhighlighted areas were the plateau regime where the current density does not increase with increasing deposition time.

Nine different loadings of three NiOOH-based catalysts, NiOOH, NiFeOOH, and NiCeOOH, were prepared by cathodic electrodeposition on GC and Au substrates (Figure S2). The first CV cycles of the catalysts deposited for 10 s are presented in Figure 1a and the overpotentials required to reach 10 mA/cm^2 for catalysts with varying loading are shown in Figure 1b. At 10 mA/cm^2, the OER activities of the samples are ordered as follows: NiOOH/GC < NiOOH/Au < NiCeOOH/GC << NiFeOOH/GC ≤ NiFeOOH/Au ≤ NiCeOOH/Au. To reach 10 mA/cm^2, the most active catalysts were 20 s deposited NiCeOOH/Au and 25 s deposited NiFeOOH/Au, requiring overpotentials as low as 259 mV and 267 mV, respectively (Figure 1b). At higher overpotentials, NiFeOOH/Au exhibits the highest activity due to its smaller Tafel slope of 39 ± 2 mV/dec compared to 90 ± 3 mV/dec of NiCeOOH/Au (Figure S3). An average measured value of 140 mA/cm^2 was achieved by 30 s deposited NiFeOOH on a flat Au surface at 300 mV overpotential in 1 M NaOH. This performance is one of the highest OER activities reported for a catalyst synthesized on a planar support (Figure 1d).[9, 14]

These activities demonstrate that a Au substrate is advantageous compared to a GC substrate in regard to the geometric activity of the NiOOH-based OER catalysts prepared by cathodic deposition, as expected from previous studies.[19] Interestingly, the enhanced activity was more pronounced at high loadings (greater than 500 nmol/cm^2), as shown in the geometric current density plots of NiOOH, NiFeOOH, and NiCeOOH at overpotentials of 400 mV, 300 mV, and 300 mV, respectively (Figure 1c-e). Up to a 6-fold increase in geometric current density was achieved by NiCeOOH/Au compared to NiCeOOH/GC.

The catalyst activities can be categorized into two regimes: the linear regime at low loadings where the activity scales linearly with the deposition time, and the plateau regime at higher loadings where the activity saturates. These linear regimes are highlighted in Figure 1c-e. The trend in

geometric area normalized activity for the two substrates in the low loading regime is mostly similar for all catalysts; activities were mostly independent of substrate. However, the transition to the plateau regime on Au substrates occurred much later compared to that on the GC substrates. This leads to a considerably higher activity on Au substrates at high loadings. We note that the geometric activity is highly dependent on the true loading of the catalysts, which can vary drastically between samples, especially at very high loadings. In order to gain deeper insights into the role of the substrate, we proceed forward by investigating the turnover frequency (TOF) normalizing activity to the total number of metal sites, a relevant metric for the intrinsic activity.

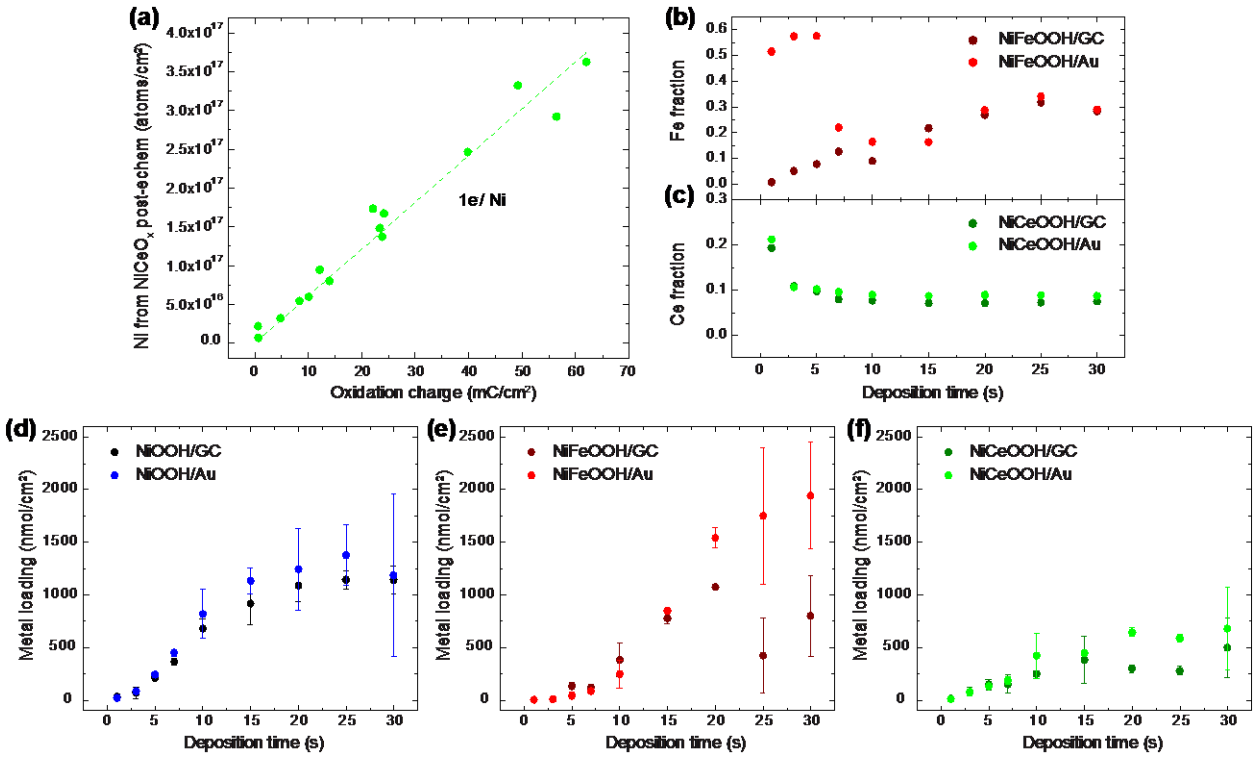

Figure 2. (a) The numbers of Ni atoms measured by ICP-OES on post-electrochemically tested NiCeOOH samples scale linearly with the charge integrated from the oxidation peak of $Ni^{2+/3+}$ with the slope of 1 e^-/Ni atom. (b) The Fe fraction of the total number of metal atoms in NiFeOOH and (c) the Ce fraction of the total number of metal atoms in NiCeOOH vary slightly with the

deposition time. Using the oxidation charge and ICP composition, the apparent metal loadings of (d) NiOOH, (e) NiFeOOH, and (f) NiCeOOH can be calculated.

3.2 Catalyst Loading Quantification and Substrate Effects on TOF

For the purpose of this discussion, we compare catalyst activity based on a turnover frequency ($TOF_{all\text{-}metal}$) that is defined such that all metal sites loaded onto the electrode contribute equally to the current. To calculate the $TOF_{all\text{-}metal}$ of the catalysts, the actual metal loading must be quantified. Using ICP-OES, the metal loadings and the Ce and Fe fractions can be measured as a function of the deposition time (Figure S4). The total amount of metal loadings (Ni, Fe, Ce) in the as-deposited films was independent of substrate. The amount of metal deposited scaled mostly linearly with the amount of charge passed during the deposition. Depending on the catalysts, the deposition efficiencies were 87-100% (Figure S4a). However, the post-electrochemical testing samples exhibited much lower metal loading than the as-deposited samples, especially in the case of high loading catalysts (Figure S4b). This implies that not all the deposited catalyst remained physically attached during the electrochemical testing. To quantify the true loading, which is the amount of catalyst that was physically adhered and electrically connected to the substrate, the number of Ni atoms can be calculated from the $Ni^{2+/3+}$ oxidation peak in the first CV cycle of the freshly deposited sample. These oxidation charges were found to track well with the amount of Ni in NiCeOOH post-electrochemically tested as measured by ICP-OES, with one transferred electron corresponding to one Ni atom, which is in excellent agreement with previous reports [22, 40] (Figure 2a).

Another critical parameter obtained from ICP-OES is the composition of the films. Figure 2b shows that Fe preferentially deposits on Au vs GC substrates, making the first portions of the

deposited film, closest to the Au substrate, to be Fe-rich up to 60% in composition. However, for depositions longer than 7 s, the Fe composition reaches a similar fraction of ~30% on both substrates. On the contrary, the composition of NiCeOOH seems to be independent of substrate and 10% Ce was observed in all films except the thinnest film of 1 s deposition, where up to 20% Ce was measured (Figure 2c). Unlike previous studies that reported drastic variations in Fe compositions in NiFeOOH films synthesized by a continuous cathodic deposition,[22] our films exhibited low variation in metal compositions, possibly due to a deposition current that is much higher. This relatively constant metal composition helps to facilitate an even distribution of OER activity in our films and simplifies the intrinsic activity analysis. Using a combination of oxidation charge and the known compositions from ICP-OES, the true amounts of catalysts at different deposition times are shown in Figure 2d-f. It is apparent that using Au substrates results in higher catalyst loadings as compared to using GC substrates, especially at longer deposition times. This is likely a result of stronger physical adhesion and higher electrical connection of the catalysts on Au.

The $TOF_{all\text{-}metal}$ values calculated from the geometric current densities and true catalyst loadings are shown in Figure 3a-c. We observed an initial decrease followed by a plateau in $TOF_{all\text{-}metal}$ as a function of deposition time which is similar to the trend observed by a previous study where the mass activity decreases as the catalyst transitions from the particle sintering regime to the constant intrinsic activity regime.[15] Nevertheless, the physical adhesion cannot be the only source of enhanced activity. Figure 3d shows that after accounting for the loading differences, the intrinsic activities of NiOOH, NiFeOOH, and NiCeOOH on Au substrate exhibit non-negligible enhancement, especially at high loadings. Up to 3 times $TOF_{all\text{-}metal}$ improvement was achieved by both NiFeOOH/Au and NiCeOOH/Au over the GC substrates.

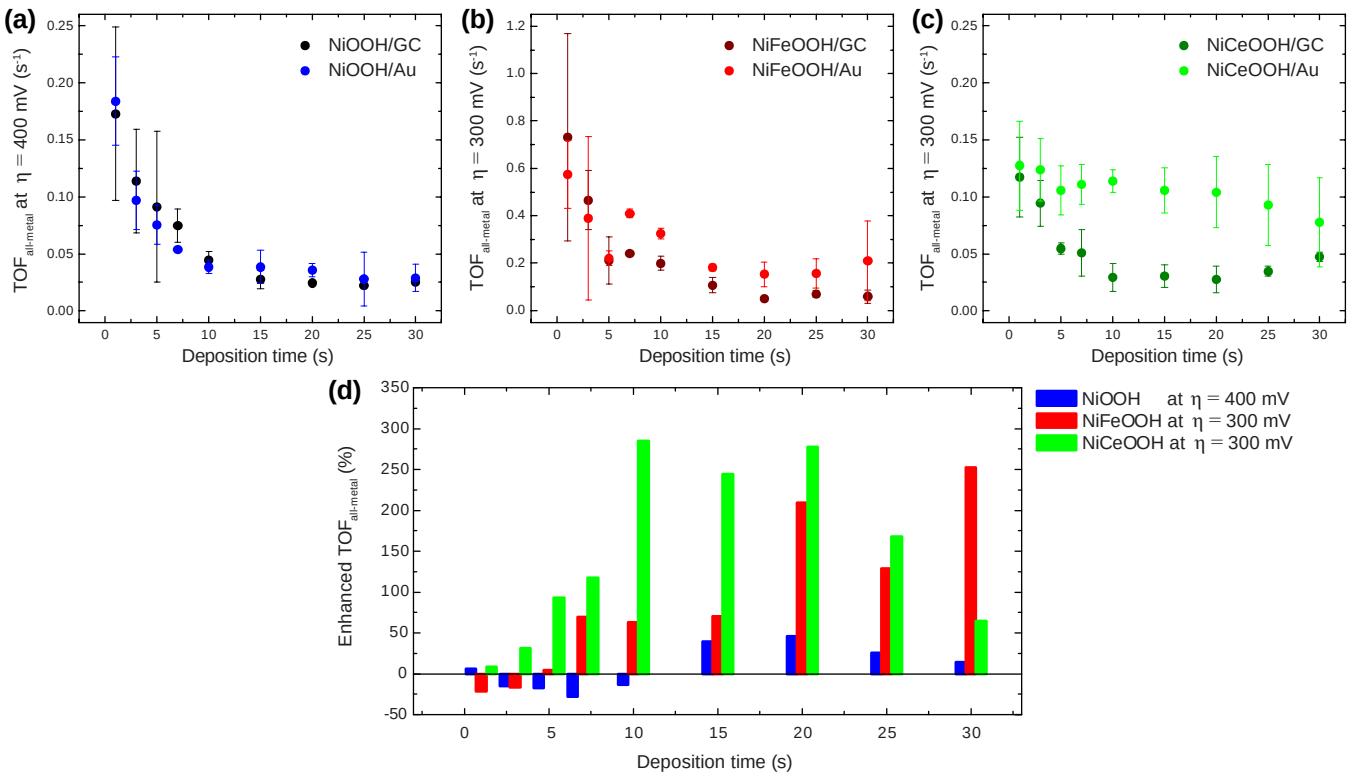

Figure 3. Average turnover frequency ($TOF_{all\text{-}metal}$) plots of (a) NiOOH, (b) NiFeOOH, and (c) NiCeOOH at the specified overpotential (η) calculated from the current densities and metal loadings from Figure 1 and 2. (d) The percentage increase in $TOF_{all\text{-}metal}$ of catalysts deposited on Au compared to GC substrate shows that Au slightly enhances the activity of NiOOH and only at high loadings for NiFeOOH but drastically improves the NiCeOOH activity for all loadings.

3.3 Electrochemical and Physical Characterizations

To investigate the origin of the enhanced activity by Au substrate, we further characterized all three catalyst systems. Without the applied potential, the catalysts are in an inactive reduced state of Ni^{2+}, indicated by the transparency of the films by eye. In order to characterize the active films, *in situ* characterization techniques are required.

3.3.1 Electrochemical Impedance Spectroscopy (EIS)

Using EIS, we investigated NiOOH, NiCeOOH, and NiFeOOH in their active states under an anodic applied bias. EIS allows us to get *in situ* information on, for example, the electrochemical surface area at OER relevant applied potentials. Figure 4a-b shows the Nyquist impedance spectra of various loadings of NiCeOOH on Au and GC substrates (see the Nyquist plots of NiOOH and NiFeOOH in Figure S5). For the ease of comparison, the electrolyte resistance (R_e) obtained at the high frequency was subtracted from each spectrum. Figure S6 shows the associated Bode plots of NiCeOOH. All Nyquist plots exhibit one or two semicircular responses, inferring that up to two characteristic time constants can be extracted.

The equivalent circuit for OER impedance spectra proposed by previous studies[41-44] and adopted by many OER studies is illustrated in Figure 4c.[15, 45] The high frequency resistive response, R_e, represents the ohmic loss from electrolyte resistance. Q_{dl} and α_{dl} are the components of a constant phase element (CPE) that represents a double layer capacitance (C_{dl}). R_p and R_s are connected to the kinetics of the interfacial charge transfer reaction. $Q_{ø}$ and $\alpha_{ø}$ are associated with the capacitive response caused by the absorbed intermediates. Lastly, R_f relates to the ohmic drop caused by the film resistivity or the electrolyte resistance drop due to porous morphology of the film,[46] and the CPE components, Q_f and α_f, are associated with the dielectric properties of the oxide film.[41] This equivalent circuit does not account for the effects of resistance loss as a function of the distance from the substrate. More complex equivalent circuits[47-48] are required to extract the absolute values of the film resistances (see further discussion in the Supporting Information). The quantitative parameters extracted from the equivalent circuit in Figure 4c are meant to establish trends for comparison within the data set.

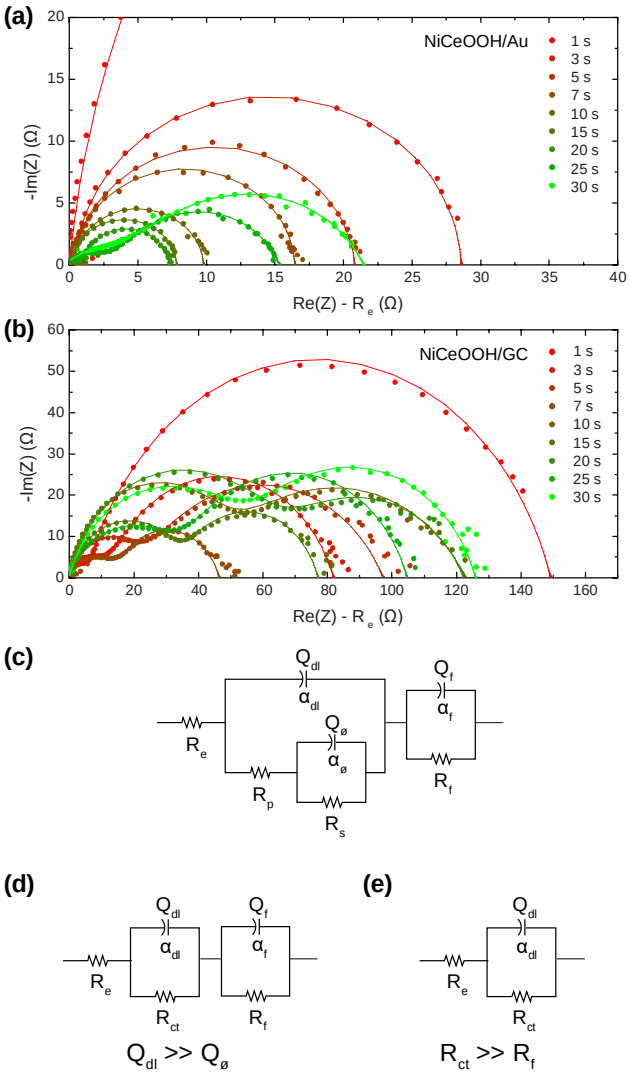

Figure 4. Nyquist plots of the (a) NiCeOOH/Au and (b) NiCeOOH/GC impedance spectra at varying deposition times. The symbols represent raw data, and the lines are the simulated spectra. For ease of comparison, the electrolyte resistance (R_e) was subtracted from the total impedance. (c) Equivalent circuit representing OER impedance. (d) Simplified model to Voigt circuit, assuming minimal effect of adsorption and desorption of intermediates. (e) The model can be reduced further to the Randles circuit by assuming no potential drop along the through-plane direction of the catalyst.

Figure 4c circuit represents an impedance spectrum with three characteristic time constants (τ = RC),[49] which was not observed in our experiment. The model can be reduced to a Voigt circuit with two characteristic time constants by assuming $Q_{ø} << Q_{dl}$ which takes place when there is negligible change in intermediate coverage due to the AC signal (Figure 4d).[41] This is a reasonable assumption because the applied potential during EIS measurement was relatively high; hence, the R_p and R_s are replaced with a combined charge transfer resistance, R_{ct}. Lastly, the model can be reduced further to a Randles circuit by assuming $R_f << R_{ct}$. This is true in the case of an ideal catalyst that has a negligible resistance loss in the film layer (Figure 4e).[41]

The Nyquist spectra of the thin loading of NiCeOOH/Au in Figure 4a show one semicircular response, inferring one characteristic time constant which is a result of the faradaic process of OER. Due to the thin and conductive catalyst, minimal potential drop occurs in the catalyst layer (negligible R_f). Thus, the Randles circuit is representative of these spectra. On the other hand, in the higher loading films, i.e. greater than 20 s deposition, two semicircle profiles are observed, which signifies two time constants were present in the spectra. The second semicircle at high frequency arises from the catalyst film itself, and spectra can be described by the Voigt model. In the case of NiCeOOH/GC, two time constants were present in all spectra regardless of the catalyst loading (Figure 4b). Similar trends were found in NiOOH and NiFeOOH systems (Figure S5).

The fitted EIS parameters can be found in Figure S7. Three important parameters will be discussed in detail: R_f represents the ohmic loss in the catalyst layer, R_{ct} describes the rate of charge transfer and can be used to calculated an instantaneous Tafel slope, and C_{dl} relates to the electrochemical surface area.

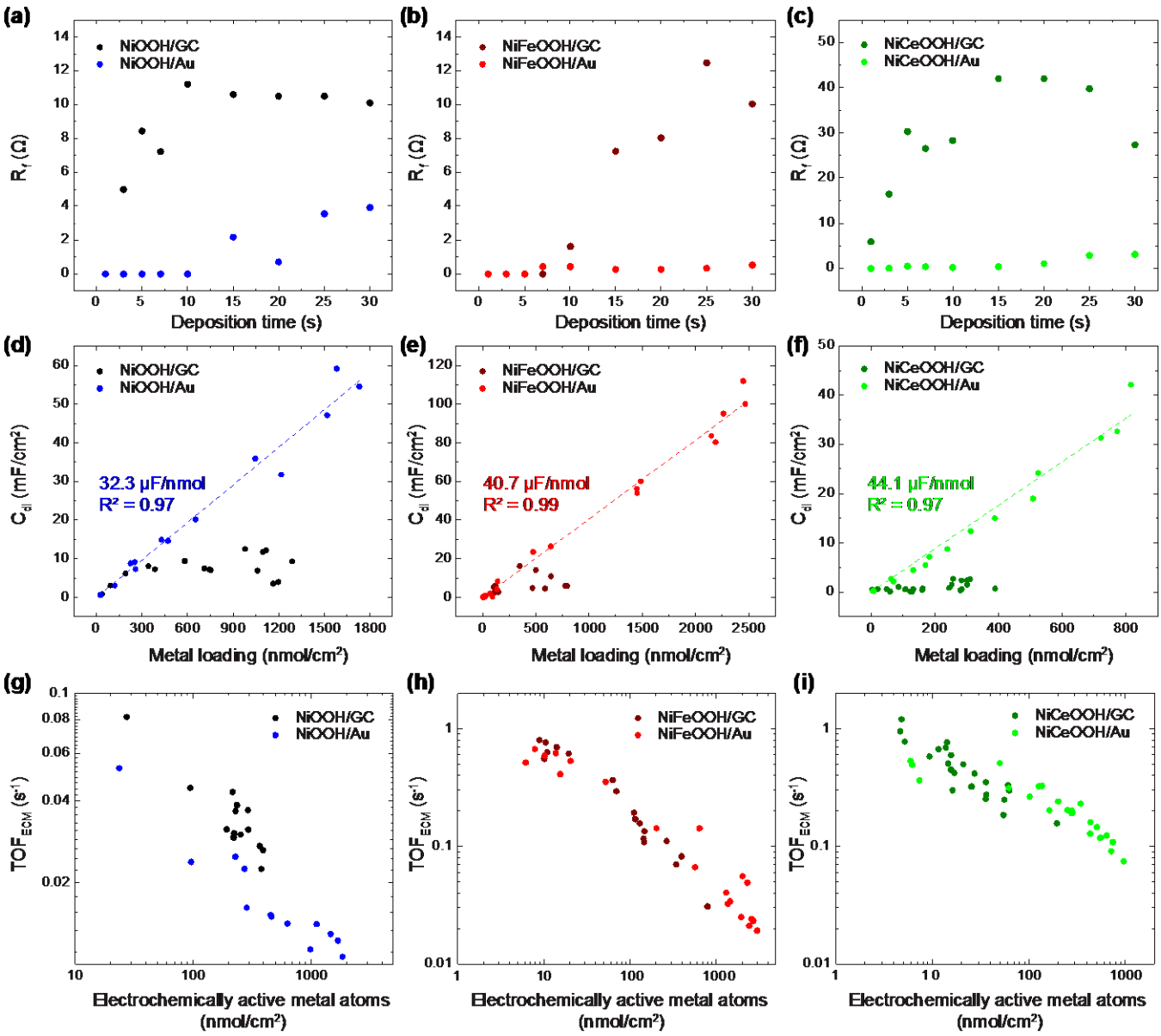

Figure 5. (a-c) R_f values obtained from the fitted EIS spectra of NiOOH, NiFeOOH, and NiCeOOH show much higher resistance on the GC substrates. (d-f) C_{dl} values of NiOOH, NiFeOOH, and NiCeOOH show that the C_{dl} values of GC samples do not linearly scale with metal loading. (g-i) Log-log plot of TOF_{ECM} (normalized to the electrochemically active metal sites) vs. electrochemically active metal calculated from C_{dl} and the current density measured during the EIS experiments of NiOOH (at 1.70 V), NiFeOOH (at 1.55 V), and NiCeOOH (at 1.60 V), showing

similar activity per electrochemically active metal site between catalysts deposited on Au and GC substrates.

The R_f values for all the catalysts deposited on Au and GC substrates share a similar trend, as shown in Figure 5a-c. On Au substrates, the R_f values of all of the catalysts were negligible in the films deposited for 10 s or shorter but became apparent in the thicker films. Nevertheless, the maximum resistance was less than 5 Ω for NiOOH/Au and NiCeOOH/Au, and it was lower than 1 Ω for NiFeOOH/Au. On the other hand, the GC substrates exhibit much higher R_f, even at low loadings. The maximum R_f values of NiOOH/GC and NiFeOOH/GC were 10 – 15 Ω, while up to 45 Ω was found on NiCeOOH/GC.

The R_f values agree very well with the trend in Tafel slopes as shown in Figure S3c-d, which was extracted from the linear regime in the Tafel plots (see Figure S3a-b for the Tafel plots of 5 s deposited and 10 s deposited catalysts). The apparent Tafel slopes of the catalyst on Au remain relatively constant, but the Tafel slopes of the catalysts on GC substrates increase drastically with the catalyst loading. This change in apparent Tafel slopes could arise from the ohmic drop in the catalyst layer, which is not a characteristic of the OER kinetics. The kinetic Tafel slope can be calculated from R_{ct} using this expression:[41]

$$\text{Tafel slope} = 2.303 i R_{ct}$$

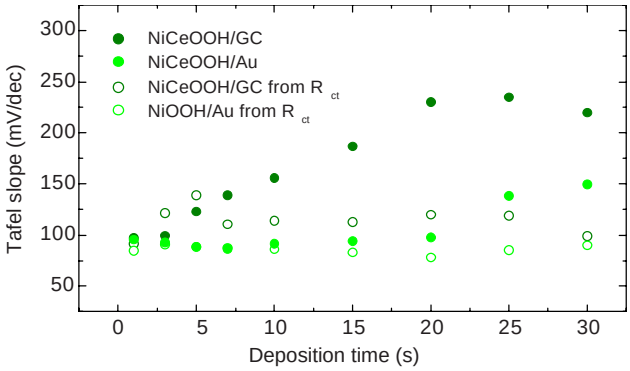

Figure 6. Tafel slopes calculated from the CV and R_{ct} values of NiCeOOH on GC and Au substrates.

Figure 6 shows that while the apparent Tafel slopes of NiCeOOH/GC varied drastically with the loading, the calculated kinetic Tafel slopes were mostly constant. This confirms that the change in the apparent Tafel slopes was not because of a change in reaction mechanism but rather from the ohmic loss due to the film resistivity. Film resistance is detrimental to the OER performance because the active sites located far away from the substrate will experience much lower applied potential. Hence, not all the metal sites were active during the electrochemical testing.

The loss in catalyst sites can be quantified by the C_{dl} extracted from the impedance spectra. The specific capacitance per metal loading can be obtained by plotting C_{dl} against the total metal loading calculated from the oxidation peak integration (Figure 5d-f). C_{dl} of the catalysts deposited on Au scales linearly with the metal loading, demonstrating a specific capacitance of 32 µF/nmol of Ni in NiOOH, 41 µF/nmol of Ni and Fe in NiFeOOH, and 44 µF/nmol of Ni and Ce in NiCeOOH. On the contrary, the C_{dl} of the catalysts on GC substrates scales linearly with the amount of metal across only the low loading regime. The C_{dl} then reaches a plateau regime. The transitions from the linear regime to the plateau regime in NiOOH/GC and NiFeOOH/GC are at

300 nmol/cm^2. This loading is equivalent to ~200 layers of NiOOH sheet, assuming a double layer hydroxide structure. Interestingly, the C_{dl} of NiCeOOH/GC barely increases with the metal loading, showing an average capacitance of 1 mF/cm^2, which corresponds to only ~15 layers of NiOOH sheet. Since the EIS measurement was performed at higher potentials than the $Ni^{2+/3+}$ oxidation potential (at 1.70 V for NiOOH, 1.55 V for NiFeOOH, and 1.60 V for NiCeOOH), it is possible that the breakdown of the linear trend on GC substrates only take places at high potential and not all oxidized Ni atoms contribute to the C_{dl} at high potentials.

Using the C_{dl} values and the aforementioned specific capacitances obtained from the Au samples, we can obtain the amount of electrochemically active metal sites from each catalyst sample. The TOF per electrochemical active metal site (TOF_{ECM}) can be calculated from the EIS measurements in which both the OER current and the number of electrochemically active metal sites are measured, and the results are shown in Figure 5g-i. The log-TOF_{ECM} vs log-electrochemically active metal sites plots show linearly decreasing trends, nearly indistinguishable between Au or GC substrates. Within the error of the measurement, we can conclude that the intrinsic activities of the NiOOH-based catalysts at the investigated loadings are independent of substrate.

In our previous work on electrodeposited NiCeOOH films, where we had first reported a substantial enhancement in catalytic activity on Au compared to GC substrates, several possibilities for the origins of that enhancement were mentioned, in particular modifying the oxygen binding energy, improving film conductivity, and increasing the accessibility of catalytic sites.[19] The results from this work show that the primary effect for enhanced activity on Au substrates, particularly in the high loading regime and observed in both the geometric activity as well as the $TOF_{all\text{-}metal}$, is predominantly caused by the lower film resistance and greater accessibility to electrochemically active sites.

3.3.2 *In Situ* Chemical Characterization by C-ray Absorption Spectroscopy (XAS)

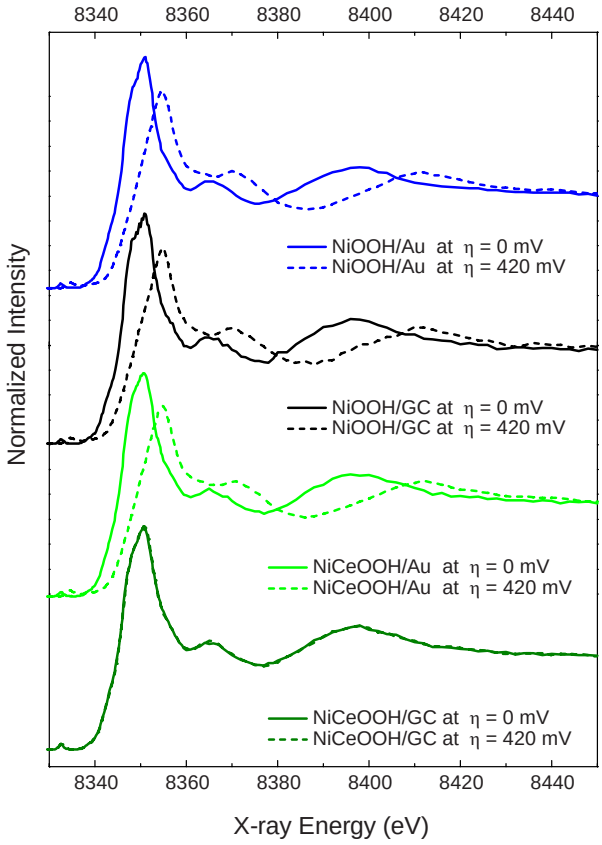

Figure 7. *In situ* XAS of NiOOH and NiCeOOH at 0 and 420 mV overpotentials on GC and Au substrates. Unlike the Ni species in NiOOH/GC, NiOOH/Au, and NiCeOOH/Au, the majority of Ni in NiCeOOH/GC did not get oxidized, resulting in low activity.

To further probe the catalyst system, the oxidation states of NiOOH and NiCeOOH on Au and GC substrates were investigated by *in situ* XAS. Samples of 1 s deposited NiOOH and NiCeOOH on GC and Au were subjected to varying applied bias from the thermodynamic OER potential to 420 mV overpotential. Figure 7 shows the XAS spectra at 0 and 420 mV overpotentials of the Ni K-edge. At zero overpotential, α-$Ni(OH)_2$ similar to the as-deposited films was present. At 420 mV overpotential, the Ni in NiOOH/GC, NiOOH/Au, and NiCeOOH/Au became oxidized and appears

to be in the γ-NiOOH phase.[50] On the contrary, the Ni species within the investigated portion of the NiCeOOH/GC sample remains at the 2+ state at 420 mV overpotential. This result has proven that there was a portion of catalyst in the NiCeOOH/GC sample that did not experience the applied potential and remained inactive throughout the experiment, which agrees with our EIS analysis.

3.3.3 Physical and Chemical Characterizations

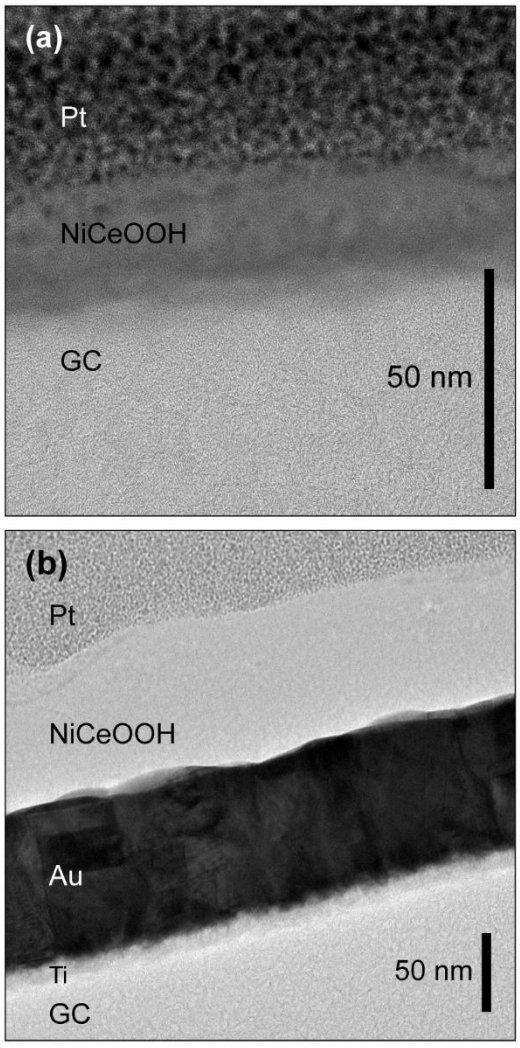

Figure 8. Cross-sectional TEM images of 10 s deposited (a) NiCeOOH/GC and (b) NiCeOOH/Au showing much thinner NiCeOOH layer on GC substrate, suggesting a highly nonhomogenous thickness which contributes to the high resistivity.

The NiCeOOH samples were characterized by AFM which shows similar morphologies between the catalysts deposited on Au and GC (Figure S8). Both films also exhibit indistinguishable surface chemical compositions confirmed by XPS, similar to our previous work.[19] The catalyst films did not show any XRD patterns. Cross-sectional TEM images of the as-prepared NiCeOOH/Au show no detectable Au diffusion into the NiCeOOH layer. However, one major difference between NiCeOOH/Au and NiCeOOH/GC is the film thickness obtained from the cross-sectional TEM images. As shown in Figure 8, the thickness of NiCeOOH on GC is ~26 nm while NiCeOOH on Au is ~78 nm. This large difference in thickness despite the similarity in loading as measured by the $Ni^{2+/3+}$ oxidation peak could be caused by the nonhomogeneity on the GC surface, resulting in a nonuniform deposition of the catalyst. This hypothesis agrees well with the difference in the deposition potential between GC and Au substrates (Figure S1). The GC substrate required greater cathodic applied potential to reach -16 mA/cm^2, which implies that the GC had a less electrochemically active surface compared to Au. The GC surface leads to a catalyst deposited with uneven thickness. The active sites located near the top of the thicker portions of the catalyst are expected to suffer from a high resistance drop. If the resistance is high enough, the catalyst might not reach a sufficiently anodic bias to drive the OER; hence, for uneven catalyst films the overall number of active sites that can participate in the reaction is lower than those for even catalyst films at the same loading. This hypothesis is confirmed by the *in situ* XAS data, which reveals that part of the NiCeOOH/GC film did not get oxidized under a very positive applied potential. The uniform, electrically conductive, and unoxidized nature of Au increases the homogeneity in electrodeposition, resulting in catalysts with lower ohmic loss, higher electrochemically active sites, and better adhesion, which leads to higher geometric activity.

4. Conclusion

We have systematically demonstrated that Au substrates enable NiOOH-based catalysts to reach much higher geometric activities at high loadings compared to GC substrates. At low overpotential, NiCeOOH/Au performed best with a loading of ~650 nmol/cm^2, requiring only 259 mV overpotential to achieve 10 mA/cm^2. At high potential, ~1800 nmol/cm^2 of NiFeOOH/Au performed best due to the lower Tafel slope, achieving 140 mA/cm^2 with 300 mV. To investigate the origin of this enhanced activity, we first quantified the true catalyst loading using ICP-OES and $Ni^{2+/3+}$ oxidation charge. ICP-OES not only verified that each oxidation charge integrated from the $Ni^{2+/3+}$ peak corresponded to one Ni atom but also gave the accurate Fe and Ce composition as a function of loading. Loading quantification elucidated that higher amounts of catalysts remained on the Au substrates compared to GC substrates, but loading difference did not explain the higher $TOF_{all\text{-}metal}$ found on Au samples at high loadings. EIS results uncovered that the biggest effect of using Au substrate is a lower film resistivity and a greater number of electrochemically active sites. This was identified by the linearly increasing double layer capacitances with increased loading of NiOOH-based catalysts on Au. On the contrary, the double layer capacitance did not increase beyond ~200 layers of NiOOH/GC and NiFeOOH/GC and only ~15 layers of NiCeOOH. This was later confirmed by *in situ* XAS, showing that NiCeOOH/GC contained a large amount of electrochemically inactive Ni species. Lastly, with cross-sectional TEM, we attributed the superior activity of NiOOH-based catalysts on Au to a more homogeneous electrodeposition, resulting in conformal films with better adhesion, lower resistivity, and higher electrochemically active metal sites. This systematic method for investigating mass activity and site specific activity as a function of loading is a way to bridge an application relevant metric such as geometric activity to the

fundamental understanding of intrinsic activity. This understanding is crucial to further engineer highly active OER catalysts for practical applications.

ASSOCIATED CONTENT

Supporting Information.

The Supporting Information is available free of charge on the ACS Publications website at DOI: 10.1021/acscatal.7b01070. The document consists of further detail on electrodeposition and electrochemical activity (Figure S1−S4), electrochemical impedance spectroscopy (Figure S5−7), and characterization by AFM (Figure S8). (PDF)

AUTHOR INFORMATION

Corresponding Author

*Email: jaramillo@stanford.edu

ACKNOWLEDGMENT

Primary support for this work was provided by the U.S. Department of Energy (DOE) Office of Science, Basic Energy Sciences to the SUNCAT Center for Interface Science and Catalysis. Use of the Stanford Synchrotron Radiation Lightsource, SLAC National Accelerator Laboratory, is supported by the U.S. Department of Energy, Office of Science, Office of Basic Energy Sciences under Contract No. DE-AC02-76SF00515. AG acknowledges the Department of Energy, Laboratory Directed Research and Development funding, under Contract No. DE-AC02-76SF00515. The authors would like to thank Dr. Desmond Ng and David Mackanic for their help with initial experiments, Tom Carver for Au physical vapor depositions, and Roy Kim for his help with the sample preparation for TEM. Characterizations were performed in Stanford

Nano Shared Facilities (SNSF) which receives support from the National Science Foundation (NSF) through the National Nanotechnology Coordinated Infrastructure (NNCI) program.
The authors declare no competing financial interest.

REFERENCES

(1) Montoya, J. H.; Seitz, L. C.; Chakthranont, P.; Vojvodic, A.; Jaramillo, T. F.; Norskov, J. K. *Nat. Mater.* 2017, *16*, 70-81.

(2) Lewis, N. S.; Nocera, D. G. *Proc. Natl. Acad. Sci. U. S. A.* 2006, *103*, 15729-15735

(3) Ng, J. W. D.; Gorlin, Y.; Hatsukade, T.; Jaramillo, T. F. *Adv. Energy Mater.* 2013, *3*, 1545-1550.

(4) Siahrostami, S.; Verdaguer-Casadevall, A.; Karamad, M.; Deiana, D.; Malacrida, P.; Wickman, B.; Escudero-Escribano, M.; Paoli, E. A.; Frydendal, R.; Hansen, T. W.; Chorkendorff, I.; Stephens, I. E. L.; Rossmeisl, J. *Nat. Mater.* 2013, *12*, 1137-1143.

(5) Bruce, P. G.; Freunberger, S. A.; Hardwick, L. J.; Tarascon, J.-M. *Nat. Mater.* 2012, *11*, 19-29.

(6) McCrory, C. C. L.; Jung, S.; Peters, J. C.; Jaramillo, T. F. *J. Am. Chem. Soc.* 2013, *135*, 16977-16987.

(7) Ayers, K. E.; Anderson, E. B.; Capuano, C.; Carter, B.; Dalton, L.; Hanlon, G.; Manco, J.; Niedzwiecki, M. *ECS Trans.* 2010, *33*, 3-15.

(8) Carmo, M.; Fritz, D. L.; Mergel, J.; Stolten, D. *Int. J. Hydrogen Energy* 2013, *38*, 4901-4934.

(9) Dionigi, F.; Strasser, P. *Adv. Energy Mater.* 2016, *6*, 1600621-n/a.

(10) Lu, X.; Zhao, C. *Nat. Commun.* 2015, *6*, 6616.

(11) Hong, W. T.; Risch, M.; Stoerzinger, K. A.; Grimaud, A.; Suntivich, J.; Shao-Horn, Y. *Energy Environ. Sci.* 2015, *8*, 1404-1427.

(12) Man, I. C.; Su, H.-Y.; Calle-Vallejo, F.; Hansen, H. A.; Martínez, J. I.; Inoglu, N. G.; Kitchin, J.; Jaramillo, T. F.; Nørskov, J. K.; Rossmeisl, J. *ChemCatChem* 2011, *3*, 1159-1165.

(13) Benck, J. D.; Hellstern, T. R.; Kibsgaard, J.; Chakthranont, P.; Jaramillo, T. F. *ACS Catal.* 2014, *4*, 3957-3971.

(14) Seh, Z. W.; Kibsgaard, J.; Dickens, C. F.; Chorkendorff, I.; Nørskov, J. K.; Jaramillo, T. F. *Science* 2017, *355*.

(15) Morales-Guio, C. G.; Liardet, L.; Hu, X. *J. Am. Chem. Soc.* 2016, *138*, 8946-8957.

(16) Subbaraman, R.; Tripkovic, D.; Chang, K.-C.; Strmcnik, D.; Paulikas, A. P.; Hirunsit, P.; Chan, M.; Greeley, J.; Stamenkovic, V.; Markovic, N. M. *Nat. Mater.* 2012, *11*, 550-557.

(17) Gong, M.; Dai, H. *Nano Res.* 2015, *8*, 23-39.

(18) Corrigan, D. A.; Bendert, R. M. *J. Electrochem. Soc.* 1989, *136*, 723-728.

(19) Ng, J. W. D.; García-Melchor, M.; Bajdich, M.; Chakthranont, P.; Kirk, C.; Vojvodic, A.; Jaramillo, T. F. *Nat. Energy* 2016, *1*, 16053.

(20) Enman, L. J.; Burke, M. S.; Batchellor, A. S.; Boettcher, S. W. *ACS Catal.* 2016, *6*, 2416-2423.

(21) Louie, M. W.; Bell, A. T. *J. Am. Chem. Soc.* 2013, *135*, 12329-12337.

(22) Batchellor, A. S.; Boettcher, S. W. *ACS Catal.* 2015, *5*, 6680-6689.

(23) Klingan, K.; Ringleb, F.; Zaharieva, I.; Heidkamp, J.; Chernev, P.; Gonzalez-Flores, D.; Risch, M.; Fischer, A.; Dau, H. *ChemSusChem* 2014, *7*, 1301-1310.

(24) Pérez-Alonso, F. J.; Adán, C.; Rojas, S.; Peña, M. A.; Fierro, J. L. G. *Int. J. Hydrogen Energy* 2014, *39*, 5204-5212.

(25) Xu, Y.; Hao, Y.; Zhang, G.; Lu, Z.; Han, S.; Li, Y.; Sun, X. *RSC Adv.* 2015, *5*, 55131-55135.

(26) Benck, J. D.; Pinaud, B. A.; Gorlin, Y.; Jaramillo, T. F. *PLoS One* 2014, *9*, e107942.

(27) Yeo, B. S.; Bell, A. T. *J. Phys. Chem. C* 2012, *116*, 8394-8400.

(28) Burke, M. S.; Zou, S.; Enman, L. J.; Kellon, J. E.; Gabor, C. A.; Pledger, E.; Boettcher, S. W. *J. Phys. Chem. Lett.* 2015, *6*, 3737-3742.

(29) Long, X.; Li, J.; Xiao, S.; Yan, K.; Wang, Z.; Chen, H.; Yang, S. *Angew. Chem., Int. Ed.* 2014, *53*, 7584-7588.

(30) Gong, M.; Li, Y.; Wang, H.; Liang, Y.; Wu, J. Z.; Zhou, J.; Wang, J.; Regier, T.; Wei, F.; Dai, H. *J. Am. Chem. Soc.* 2013, *135*, 8452-8455.

(31) Yu, X.; Zhang, M.; Yuan, W.; Shi, G. *J. Mater. Chem. A* 2015, *3*, 6921-6928.

(32) Klaus, S.; Cai, Y.; Louie, M. W.; Trotochaud, L.; Bell, A. T. *J. Phys. Chem. C* 2015, *119*, 7243-7254.

(33) Yeo, B. S.; Bell, A. T. *J. Am. Chem. Soc.* 2011, *133*, 5587-5593.

(34) Zou, S.; Burke, M. S.; Kast, M. G.; Fan, J.; Danilovic, N.; Boettcher, S. W. *Chem. Mater.* 2015, *27*, 8011-8020.

(35) Gorlin, Y.; Chung, C. J.; Benck, J. D.; Nordlund, D.; Seitz, L.; Weng, T. C.; Sokaras, D.; Clemens, B. M.; Jaramillo, T. F. *J. Am. Chem. Soc.* 2014, *136*, 4920-4926.

(36) Seitz, L. C.; Hersbach, T. J. P.; Nordlund, D.; Jaramillo, T. F. *J. Phys. Chem. Lett.* 2015, *6*, 4178-4183.

(37) Trotochaud, L.; Young, S. L.; Ranney, J. K.; Boettcher, S. W. *J. Am. Chem. Soc.* 2014, *136*, 6744-6753.

(38) Lasia, A. Electrochemical impedance spectroscopy and its applications; Springer: 2014; pp 177-250.

(39) Sokaras, D.; Weng, T.-C.; Nordlund, D.; Alonso-Mori, R.; Velikov, P.; Wenger, D.; Garachtchenko, A.; George, M.; Borzenets, V.; Johnson, B. *Rev. Sci. Instrum.* 2013, *84*, 053102.

(40) Stevens, M. B.; Enman, L. J.; Batchellor, A. S.; Cosby, M. R.; Vise, A. E.; Trang, C. D. M.; Boettcher, S. W. *Chem. Mater.* 2017, *29*, 120.

(41) Lyons, M. E.; Brandon, M. P. *J. Electroanal. Chem.* 2009, *631*, 62-70.

(42) Doyle, R. L.; Godwin, I. J.; Brandon, M. P.; Lyons, M. E. G. *Phys. Chem. Chem. Phys.* 2013, *15*, 13737-13783.

(43) Doyle, R. L.; Lyons, M. E. G. *Phys. Chem. Chem. Phys.* 2013, *15*, 5224-5237.

(44) Doyle, R. L.; Lyons, M. E. G. *J. Electrochem. Soc.* 2013, *160*, H142-H154.

(45) Swierk, J. R.; Klaus, S.; Trotochaud, L.; Bell, A. T.; Tilley, T. D. *J. Phys. Chem. C* 2015, *119*, 19022-19029.

(46) Chen, L.; Lasia, A. *J. Electrochem. Soc.* 1993, *140*, 2464-2473.

(47) Bisquert, J. *J. Phys. Chem. B* 2002, *106*, 325-333.

(48) Bisquert, J.; Grätzel, M.; Wang, Q.; Fabregat-Santiago, F. *J. Phys. Chem. B* 2006, *110*, 11284-11290.

(49) Orazem, M. E.; Tribollet, B. Electrochemical impedance spectroscopy; John Wiley & Sons: 2011; Vol. 48, pp 233-264.

(50) Friebel, D.; Louie, M. W.; Bajdich, M.; Sanwald, K. E.; Cai, Y.; Wise, A. M.; Cheng, M.-J.; Sokaras, D.; Weng, T.-C.; Alonso-Mori, R.; Davis, R. C.; Bargar, J. R.; Nørskov, J. K.; Nilsson, A.; Bell, A. T. *J. Am. Chem. Soc.* 2015, *137*, 1305-1313.

TOC Graphic

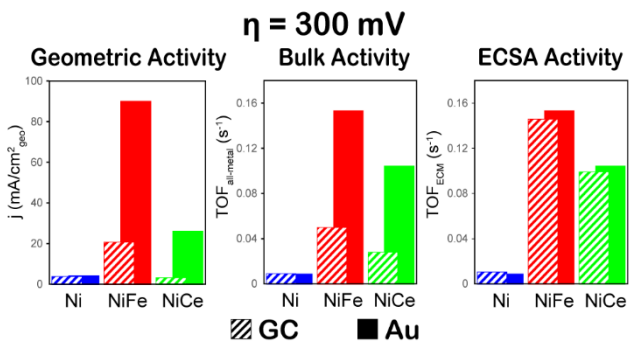
η = 300 mV
Geometric Activity
Bulk Activity
ECSA Activity
j (mA/cm2geo)
TOFall-metals (s-1)
TOFECM (s-1)
Ni
NiFe
NiCe
GC
Au